AJNR

Visualization of the Medial and Lateral Geniculate Nucleus on Phase Difference Enhanced Imaging

M. Kitajima, T. Hirai, T. Yoneda, Y. Iryo, M. Azuma, M. Tateishi, K. Morita, M. Komi and Y. Yamashita

AJNR Am J Neuroradiol 2015, 36 (9) 1669-1674
doi: https://doi.org/10.3174/ajnr.A4356
http://www.ajnr.org/content/36/9/1669

Visualization of the Medial and Lateral Geniculate Nucleus on Phase Difference Enhanced Imaging

M. Kitajima, T. Hirai, T. Yoneda, Y. Iryo, M. Azuma, M. Tateishi, K. Morita, M. Komi, and Y. Yamashita

ABSTRACT

BACKGROUND AND PURPOSE: The precise identification and measurement of the medial geniculate nucleus and lateral geniculate nucleus on MR imaging remain technically challenging because the thalamic nuclei are small structures. We compared the visualization of the medial geniculate nucleus and lateral geniculate nucleus on phase difference enhanced imaging with 3D high-resolution phase imaging, 2D-T2WI, STIR, proton attenuation–weighted imaging, and DTI acquired at 3T. We also measured the volume and height of the medial geniculate nucleus and lateral geniculate nucleus on phase difference enhanced imaging.

MATERIALS AND METHODS: Phase difference enhanced, 2D-T2-weighted, STIR, proton attenuation–weighted, and DTI were acquired on a 3T MR imaging unit in 10 healthy volunteers. Two neuroradiologists recorded the qualitative visualization scores of the medial geniculate nucleus and lateral geniculate nucleus, specifically the identification of their boundaries, for all images. Measurement differences were assessed with the Wilcoxon signed rank test. The volume and height of the medial geniculate nucleus and lateral geniculate nucleus were measured on phase difference enhanced imaging and compared with previously reported values.

RESULTS: The qualitative visualization scores of the lateral geniculate nucleus and medial geniculate nucleus were significantly higher on phase difference enhanced images than on T2-weighted, proton attenuation–weighted, STIR, or DTI ($P < .05$). On phase difference enhanced imaging, the medial geniculate nucleus and lateral geniculate nucleus were bordered by low-intensity structures: the cerebral peduncle, the origin of the optic radiation, and the superior and inferior quadrigeminal brachia. The volume of the medial geniculate nucleus and lateral geniculate nucleus varied from 74.0 to 183.75 mm^3 (mean, 129.0 ± 34.7 mm^3) and from 96.5 to 173.75 mm^3 (mean, 135.2 ± 28.0 mm^3), respectively.

CONCLUSIONS: For the depiction of the medial geniculate nucleus and lateral geniculate nucleus on 3T MR imaging, phase difference enhanced imaging is superior to conventional MR imaging. The medial geniculate nucleus and lateral geniculate nucleus volumes vary among individuals.

ABBREVIATIONS: LGN = lateral geniculate nucleus; MGN = medial geniculate nucleus; PADRE = phase difference enhanced; PD = proton attenuation–weighted imaging

The medial geniculate nucleus (MGN) and lateral geniculate nucleus (LGN) are the specific thalamic nuclei that relay the auditory and optic pathways, respectively. The triangular LGN is located in the posterior region of the thalamus. It is bordered anteriorly by the cerebral peduncle and the optic tract and posteriorly by the origin of the optic radiation. The oval MGN, with its long axis directed forward and laterally just medial to the LGN, is bordered anteriorly by the inferior quadrigeminal brachium and posteriorly by the superior quadrigeminal brachium. There is increasing interest in assessing the MGN and LGN in healthy subjects and in patients with ophthalmic diseases such as glaucoma.[1-6] However, current imaging methods for identifying the MGN and LGN vary, and imaging findings are inconsistent.

Technical advances in neuroimaging facilitate the study of subcortical structures in vivo. Phase difference enhanced (PADRE) imaging yields a high tissue contrast that delineates specific white matter tracts and intracortical structures.[7-9] On high-spatial-resolution 3T PADRE images, small structures, including the central tegmental tract, the medial and dorsal longitudinal fascicules, and the stria of Gennari, which are difficult to appreciate on conven-

Received May 16, 2014; accepted after revision February 10, 2015.

From the Department of Diagnostic Radiology, Graduate School of Medical Sciences (M.K., T.H., Y.I., M.A., M.T., Y.Y.) and Department of Medical Physics in Advanced Biomedical Sciences, Faculty of Life Sciences (T.Y.), Kumamoto University, Kumamoto, Japan; and Department of Radiology (K.M., M.K.), Kumamoto University Hospital, Kumamoto, Japan.

Paper previously presented at: Annual Meeting of the American Society of Neuroradiology and the Foundation of the ASNR Symposium, May 18–23, 2013; San Diego, California.

Please address correspondence to Mika Kitajima, MD, Department of Diagnostic Radiology, Graduate School of Medical Sciences, Kumamoto University, 1-1-1, Honjo, Chuo-ku, Kumamoto-shi, Kumamoto, 860-0811, Japan; e-mail: mkitaji@kumamoto-u.ac.jp

http://dx.doi.org/10.3174/ajnr.A4356

tional MR images, are delineated.[7,8] Also, the contrast between specific white matter structure (eg, the optic radiation) is higher on PADRE than on conventional MR images.[7]

We compared visualization of the MGN and LGN on PADRE, 2D-T2-weighted, STIR, proton attenuation–weighted (PD), and DTI acquired at 3T. We also measured the volume and height of the MGN and LGN on PADRE images.

MATERIALS AND METHODS

Subjects

This study was approved by our institutional review board. Informed consent was obtained from all healthy volunteers (6 men, 4 women; age range, 28–47 years; mean, 36.8 ± 6.7 years); none had a history of neurologic, psychiatric, or ophthalmologic diseases, including glaucoma.

Imaging Protocol

All measurements were performed on a 3T MR imaging scanner (Achieva; Philips Healthcare, Best, the Netherlands). A set consisting of 3D high-resolution T1 fast-field echo images for PADRE, 2D-T2-weighted, STIR, PD, and DTI was obtained in all subjects. The images were acquired in the transverse plane parallel to the anterior/posterior commissure line. The scan parameters of each sequence were the following: 3D-T1 fast-field echo images for PADRE: TR/TE, 32/23 ms; FOV, 200 mm; matrix size, 307 × 384; reconstructed matrix size, 400 × 400; spatial resolution, 0.5 × 0.5 × 1.0 mm; sensitivity encoding factor, 2; flip angle, 10°; 1 signal acquired; image acquisition time, 3 minutes 36 seconds. We also reconstructed PADRE images with a 3-mm thickness. For 2D-PD and T2-weighted images, the parameters were the following: TR/TE, 4000/17, 80 ms; FOV, 200 mm; matrix size, 280 × 400; spatial resolution, 0.4 × 0.4 mm; turbo factor, 9; sensitivity encoding, 1.5; refocusing angle, 120°; 2 signals acquired; acquisition time, 2 minutes 16 seconds to 3 minutes 20 seconds. For STIR, the parameters were the following: TR/TE, 5000/20 ms; FOV, 200 mm; matrix size, 224 × 320; TI, 120 ms; spatial resolution, 0.4 × 0.4 mm; turbo factor, 9; sensitivity encoding factor, 2.0; refocusing angle, 120°; 2 signals acquired; acquisition time, 3 minutes 10 seconds. The section thickness and gap of the 2D sequences were 3.0 and 1.0 mm, respectively. DTI was obtained with single-shot spin-echo EPI: TE, 49 ms; spatial resolution, 0.8 × 0.8 × 3.0 mm; 6 signals acquired; b-factor, 0/700 s/mm^2; EPI factor, 49. We used a tilted $\pi/2$ pulse and optimized outer-volume suppression. The image acquisition time was 11 minutes 15 seconds. Gray-scale fractional anisotropy maps were used for evaluation. On the fractional anisotropy map, areas with high degrees of fractional anisotropy (eg, internal capsule) are bright, and areas with low degrees of fractional anisotropy (eg, gray matter) are dark.

Data Processing of PADRE

The PADRE technique was described in previous reports.[8,9] One of the major concepts responsible for the power of the PADRE technique is the "phase difference selection," which enhances the magnetic properties of the target tissue. PADRE imaging classifies and selects various phase differences, $\Delta\theta$, to enhance the different tissues, and enhances all of them on the magnitude image $|\rho|$ by the enhancing function $w(\Delta\theta)$. Finally, the PADRE image ρPADRE is reconstructed as $\rho\text{PADRE} = w(\Delta\theta)\,|\rho|$.

In this study, the positive phase difference ($\Delta\theta$) was selected to enhance myelin.[7,8]

All images were calculated off-line with in-house software.

All postprocessing of DTI and PADRE images was fully automatic without user intervention to eliminate operator bias.

MGN and LGN Localization and Measurement

To evaluate the visibility of the boundaries of the MGN and LGN, 2 experienced neuroradiologists (T.H., Y.I. with 21 and 9 years of neuroradiology experience, respectively) independently assessed the original PADRE (1-mm thickness), reconstructed PADRE (3-mm thickness), 2D-T2-weighted, STIR, PD, and DTI by referring to the atlas of Schaltenbrand and Wahren[10] and *Duvernoy's*[11] atlas. They assigned MGN and LGN visualization scores to each imaging method, where 0 = no visible boundary of the nucleus, 1 = poorly visible with a fuzzy boundary, 2 = mostly visible with a slightly fuzzy boundary, and 3 = well-identified nucleus and clearly distinguishable from neighboring structures.

A third neuroradiologist (M.K. with 20 years of neuroradiology experience) subsequently measured the area of the MGN and LGN by manually outlining their boundaries on each original PADRE image section. The total volume was obtained by summing the areas of all sections. The number of sections on which the nucleus was identified was also recorded as the height of the nucleus. To assess the volume and height of the MGN and LGN, we compared our estimated volume and height based on PADRE with previously reported histologic and MR imaging measurements.[5,6,12,13]

Statistical Analysis

To assess interobserver agreement for each imaging method, we calculated the percentage of agreement as the number of subjects who received identical scores from both observers divided by the number of subjects ($n = 10$). Visualization scores were analyzed with the Wilcoxon signed rank test by using all 10 subjects to determine the difference between PADRE and each of the other imaging methods. A P value $<.05$ was statistically significant. All statistical analyses were performed with MedCalc, Version 12.7.1.0 (MedCalc for Windows, Mariakerke, Belgium).

RESULTS

Imaging was successful in all 10 subjects. In subjects with a score of >1, the triangular LGN and the ovoid MGN were slightly hyperintense on PD and STIR images (Fig 1). Although the MGNs were not identified on DTI, >90% of the LGNs were identified. On fractional anisotropy maps, the cerebral peduncle and origin of the optic radiation exhibited bright. The LGNs were identified as triangular dark areas between the cerebral peduncle and the origin of the optic radiation (Fig 1). Although 1 LGN and 2 MGNs were not identified on reconstructed PADRE due to the failure of the unwrapping of phase information, >80% of the MGNs and LGNs were well-identified and clearly differentiated from neighboring structures on both original and reconstructed PADRE imaging. Reference to the anatomic atlas and the textbook revealed that the LGN was hyperintense compared with

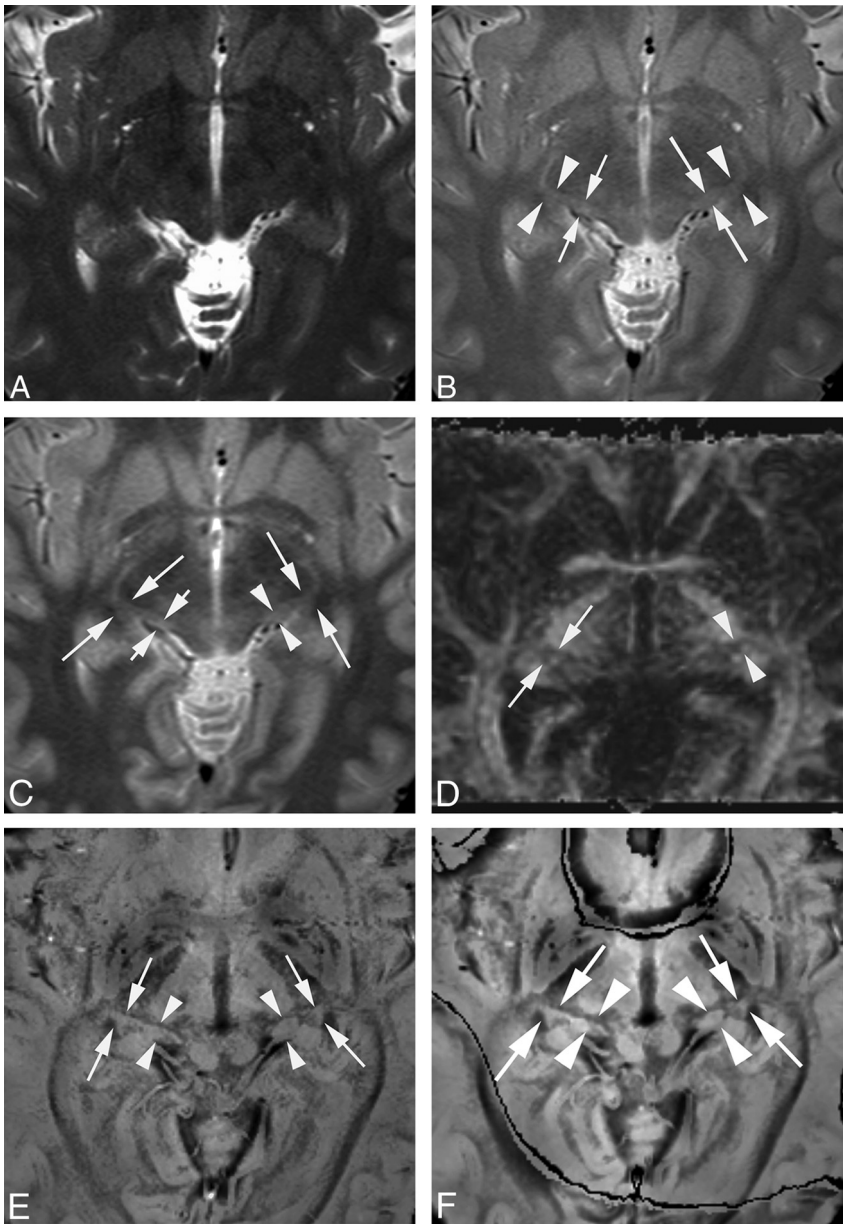

FIG 1. MGN and LGN in a healthy 31-year-old female volunteer. T2-weighted (*A*), PD (*B*), STIR (*C*), DTI (*D*), original PADRE (1 mm) (*E*), and reconstructed PADRE (3 mm) images (*F*). *A*, Neither side of the MGN or LGN is identified (visualization score = 0 by both observers). *B*, The right MGN is poorly visible. Its boundary is fuzzy (*short arrows*) (visualization score = 1 by both observers). The left MGN is mostly visible; its boundary is slightly fuzzy (*long arrows*) (visualization score = 2 by both observers). Both sides of the LGN are mostly visible; the boundary is slightly fuzzy (*arrowheads*) (visualization score = 2 by both observers). *C*, One observer assigned a visualization score of 1, the other of 2, to the right MGN (*short arrows*). The left MGN is mostly visible with a slightly fuzzy boundary (*arrowheads*) (visualization score = 2 by both observers). Both sides of the LGN are mostly visible with a slightly fuzzy border (*long arrows*) (visualization score = 2 by both observers). *D*, Neither side of the MGN is identified (visualization score = 0 by both observers). The right LGN is mostly visible with a slightly fuzzy border (*arrows*) (visualization score = 2 by both observers). The left LGN is poorly visible; its border is fuzzy (*arrowheads*) (visualization score = 1 by both observers). *E*, Both sides of the MGN (*arrowheads*) and LGN (*arrows*) are well-identified and clearly differentiated from lateral and medial neighboring structures (visualization score = 3 by both observers). *F*, Although the boundaries of the LGN and MGN are slightly obscure on reconstructed PADRE compared with the original PADRE, both sides of the MGN (*arrowheads*) and LGN (*arrows*) are well-identified and clearly differentiated from lateral and medial neighboring structures (visualization score = 3 by both observers).

surrounding structures, the cerebral peduncle and the origin of the optic radiation (Figs 1 and 2). The MGN was hyperintense compared with surrounding structures, the superior and inferior quadrigeminal brachia, which exhibited low signal intensity (Figs 1 and 2).

Statistics of the visualization scores assigned by the 2 observers are presented in Fig 3. The average scores assigned to the LGN by the 2 observers for T2-weighted, PD, STIR, DTI, and original and reconstructed PADRE images were 0.0 ± 0.0, 1.33 ± 0.57, 1.56 ± 0.64, 1.78 ± 0.77, 2.88 ± 0.33, and 2.82 ± 0.51, respectively. The average MGN scores for T2-weighted, PD, STIR, DTI, and original and reconstructed PADRE images were 0.10 ± 0.30, 0.85 ± 0.77, 1.08 ± 0.86, 0.0 ± 0.0, 2.98 ± 0.16, and 2.94 ± 0.23, respectively. For the 20 LGN scores (10 subjects), the percentage of agreement was 100.0%, 70%, 75%, 45%, 85%, and 89.5% for T2-weighted, PD, STIR, DTI, and the original and reconstructed PADRE images, respectively. For the MGN scores, the percentage of agreement was 80%, 45%, 55%, 100%, 100%, and 88.9% for T2-weighted, PD, STIR, DTI, and original and reconstructed PADRE images, respectively. The difference in scores between original PADRE and all of the other 2D images for both the LGN and MGN was statistically significant ($P < .01$). The difference in scores between reconstructed PADRE and all of the other 2D images for both the LGN and MGN was also statistically significant ($P < .05$). In contrast, we found no statistically significant difference between original and reconstructed PADRE for both the LGN and MGN.

The volume of the MGN and LGN measured on original PADRE varied among individuals; for the MGN, it ranged from 74.0 to 183.75 mm^3 (mean, 129.0 ± 34.7 mm^3), and for the LGN, 96.5–173.75 mm^3 (mean, 135.2 ± 28.0 mm^3). The height of the MGN varied from 4.0 to 7.0 mm (mean, 5.7 ± 0.88 mm); for the LGN, it varied from 4.0 to 7.0 mm (mean, 5.5 ± 0.95 mm).

DISCUSSION

Our results indicated that PADRE yielded a superior visibility of the MGN and LGN when directly compared with T2-weighted, DTI, PD, and STIR images. The superior visualization on PADRE compared with T2-weighted, PD, and STIR images may be attributable to different mechanisms of signal generation (ie, the susceptibility-based

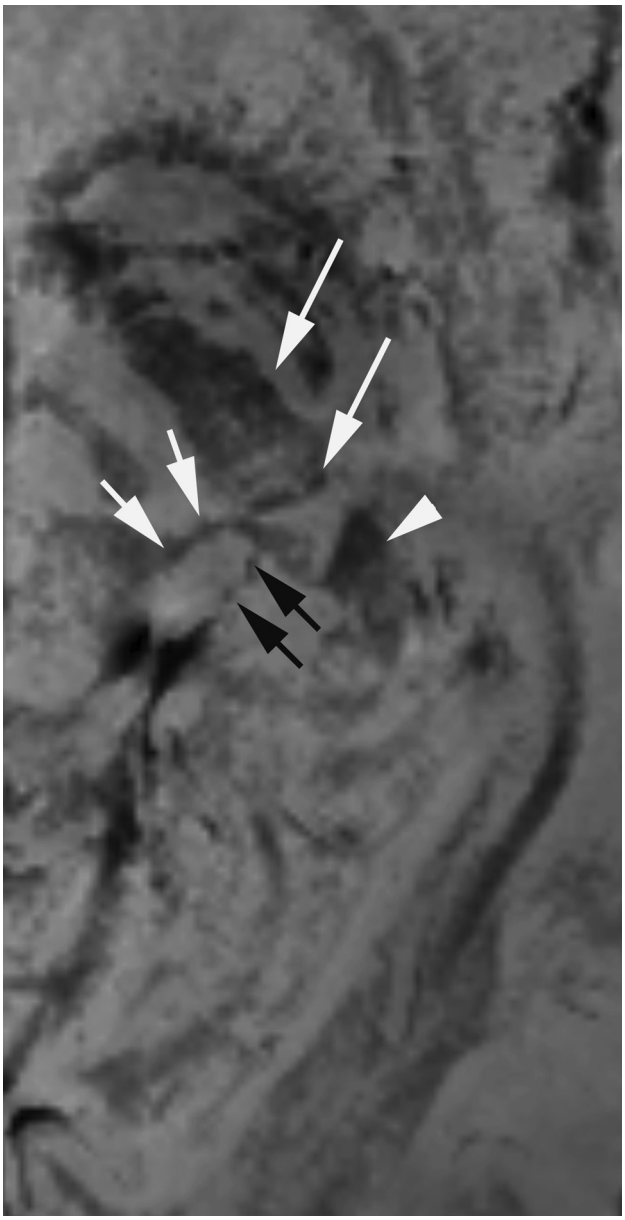

FIG 2. A magnified PADRE image of the left MGN and LGN in a healthy 28-year-old female volunteer. The left LGN is surrounded by the cerebral peduncle (*long arrows*) anteriorly and the origin of the optic radiation (*arrowhead*) posteriorly. The MGN is surrounded by the inferior (*arrows*) and superior quadrigeminal brachium (*black arrows*). The MGN and LGN are distinguished from surrounding structures with low signal intensity.

methods used in PADRE versus the relaxation-based techniques of T2-weighted, PD, and STIR). Phase images acquired with high magnetic fields (7T and above) yield information about biologic structures that are not usually identified by conventional MR imaging.[14-16] Blood deoxyhemoglobin, tissue lipid, nonheme iron content,[15] and water-protein exchange[17] have been proposed as possible origins of the MR imaging signal frequency shift responsible for the contrast on phase images. In contrast, the discrepancies between structures on relaxation-based methods originate from differences in the decay rates, which are small. Thus, high-resolution phase imaging may be able to delineate small structures that are difficult to evaluate on conventional MR images.

In addition to the comparison between original PADRE and 2D images, we also compared reconstructed PADRE and 2D sequences with nearly identical thickness. On reconstructed PADRE images, the signal-to-noise ratio becomes higher compared with original PADRE images. In contrast, the boundary between the target structures and the surrounding structures on reconstructed PADRE images becomes more obscure because of an increase in the partial volume effect. However, we found no statistically significant difference for the visualization score of LGN and MGN between original and reconstructed PADRE images.

He and Yablonskiy[18] reported that the optic radiation, a myelin-rich structure, exhibited a negative phase value in the left-handed system—that is, a positive phase value in the right-handed system used in our study. In our study, positive phase values appeared as dark signals. The fiber orientation of the optic radiation to the main magnetic field direction and the cerebral blood volume also affect the image contrast of the optic radiation on phase images.[18] Li et al[19] demonstrated that the structure of myelin and its orientation to the static magnetic field affect white matter fiber susceptibility, resulting in a negative susceptibility change. Ide et al[7] reported that the contrast between the optic radiation and the surrounding tissue on PADRE was similar to that on myelin-stained specimens. As with the optic radiation, the difference in the myelin content between the thalamic nuclei, the LGN and MGN, and their surrounding structures, specifically the cerebral peduncle, optic radiation, and the superior and inferior quadrigeminal brachia, may have affected the contrast on PADRE images. Furthermore, the fiber orientation and cerebral blood volume of those small white matter tracts also may have affected this contrast. We suggest that the high contrast between the thalamic nuclei and neighboring white matter tracts on PADRE facilitates the easy identification of the MGN and LGN.

Horton et al[20] provided the first PD images of the LGN; they performed postmortem studies and studies on living human subjects. They demonstrated a good correlation between MR images and anatomic sections. For the identification of the LGN, Fujita et al[21] documented an excellent correspondence between PD images and images obtained with functional methods by using blood oxygen level–dependent imaging. In our study, the averaged visualization scores of the LGN and MGN were higher for PD than for T2-weighted images and lower than those recorded for PADRE images. Devlin et al[22] reported a different approach for the identification of the MGN and LGN by using DTI. They used probabilistic tractography to automatically segment the 2 nuclei from surrounding structures on the basis of their distinctive patterns of connectivity to the rest of the brain. DTI data for probabilistic tractography were obtained by using a doubly refocused spin-echo sequence and cardiac gating with 60 diffusion-weighted images. These resulted in an acquisition time of approximately 20 minutes and a spatial resolution of $1.875 \times 1.875 \times 2.5\ mm^3$. They reported identifying the MGN and LGN in all of their 5 neurologically healthy volunteers. However, because probabilistic tractography requires thousands of iterations, it is computationally intensive. In contrast, PADRE images can be acquired with commonly available imaging sequences within a reasonable image acquisition time. Furthermore, PADRE provides images

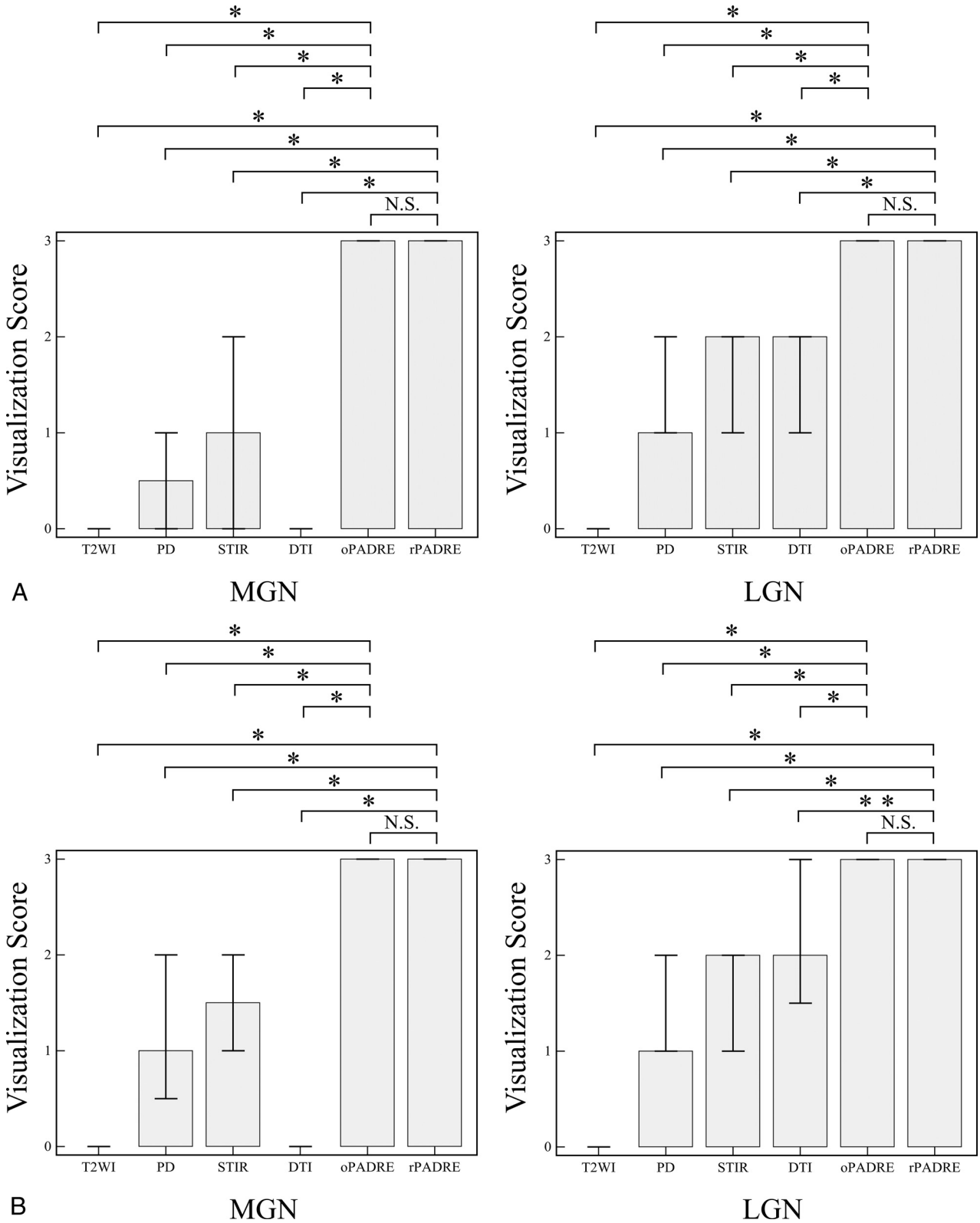

FIG 3. Graphs show the statistics for the visualization scores assigned by the 2 observers. The visualization scores of LGN and MGN are higher on original and reconstructed PADRE than those on other 2D sequences in observers 1 (*A*) and 2 (*B*). The height of the bar denotes the median, and error bars, the 25%–75% percentile. The asterisk indicates $P < .01$; double asterisks, $P < .05$ compared with PADRE; N.S.; not significant; oPADRE, original PADRE with 1-mm section thickness; rPADRE, reconstructed PADRE with 3-mm section thickness.

with high spatial resolution and low image distortion and is less computationally intensive than the probabilistic tractography technique.

The previously reported LGN volume measured on MR images in healthy subjects varied from 75.3 to 86.7 mm^3.[5,6] In a histologic study,[12] it varied from 66 to 157 mm^3; among individuals, the variation was 2- to 3-fold. In our search of the literature,

we found only 1 postmortem study on the volume of the MGN[13]; this nucleus was reported to be 5-mm wide, 4-mm high, and 4- to 5-mm long. Our volume measurements for LGN were larger than those reported in earlier MR imaging and histologic studies.[5,6,12] The height of the LGN was slightly larger than that in earlier MR imaging studies (4.7–4.8 mm), and the height of the MGN was somewhat larger than the height (4–5 mm) in the histologic investigation of Winer.[13]

We attribute the discrepancy between ours and earlier findings on the LGN and MGN to several factors: First, our study population was small. Second, differences in the identification techniques such as the blood oxygen level–dependent and spin-echo techniques used by others and our susceptibility-based technique affect volume measurements. Blooming artifacts may be more prominent on gradient-echo images such as PADRE than on spin-echo images. They depend on the orientation and geometry of the object and on various imaging parameters. Third, the volume of living and postmortem human brains removed from the skull and fixed with formalin may be different.

Measuring the LGN volume on MR imaging may be of clinical importance. According to earlier MR imaging studies, the volume of LGN decreases with age.[6] In patients with glaucoma, the LGN height and volume are diminished and the extent of atrophy of the LGN is correlated with the clinical stage.[1,5] We believe that the PADRE technique reinforces the clinical utility of MR imaging in the diagnosis of diseases involving the LGN and MGN. Prospective clinical studies are underway in our laboratory to confirm the utility of PADRE.

Our study has some limitations. First, all of our subjects were healthy young Japanese adults. Our findings may not be applicable to other populations or age groups. Because the volume of the LGN varies 2- to 3-fold among individuals, additional qualitative and quantitative studies of the MGN and LGN on PADRE images are required in larger independent series comprising healthy subjects and patients with diseases affecting the MGN and LGN. Second, we did not compare the visualization of the nuclei directly between the original PADRE and other 3D sequences at identical spatial resolutions. Further studies of comparison between PADRE and other 3D sequences at identical spatial resolutions are required. In addition to the direct comparison, registration of all the sequences with transparent overlay may be useful to evaluate the differences of the LGN and MGN visualization among the sequences.

CONCLUSIONS

On PADRE images, visualization of the MGN and LGN is significantly better than that on current standard MR imaging sequences. Therefore, PADRE is useful for the localization of the MGN and LGN.

Disclosures: Tetsuya Yoneda—*RELATED*: *Grant*: Philips Healthcare,* *Comments*: joint research; *UNRELATED*: *Royalties*: Philips Healthcare,* *Comments*: development of SWI with phase enhancement. *Money paid to the institution.

REFERENCES

1. Dai H, Mu KT, Qi JP, et al. **Assessment of lateral geniculate nucleus atrophy with 3T MR imaging and correlation with clinical stage of glaucoma.** *AJNR Am J Neuroradiol* 2011;32:1347–53
2. O'Connor DH, Fukui MM, Pinsk MA, et al. **Attention modulates responses in the human lateral geniculate nucleus.** *Nat Neurosci* 2002;5:1203–09
3. Selemon LD, Begovic A. **Stereologic analysis of the lateral geniculate nucleus of the thalamus in normal and schizophrenic subjects.** *Psychiatry Res* 2007;151:1–10
4. Hess RF, Thompson B, Gole G, et al. **Deficient responses from the lateral geniculate nucleus in humans with amblyopia.** *Eur J Neurosci* 2009;29:1064–70
5. Gupta N, Greenberg G, de Tilly LN, et al. **Atrophy of the lateral geniculate nucleus in human glaucoma detected by magnetic resonance imaging.** *Br J Ophthalmol* 2009;93:56–60
6. Li M, He HG, Shi W, et al. **Quantification of the human lateral geniculate nucleus in vivo using MR imaging based on morphometry: volume loss with age.** *AJNR Am J Neuroradiol* 2012;33:915–21
7. Ide S, Kakeda S, Korogi Y, et al. **Delineation of optic radiation and stria of Gennari on high-resolution phase difference enhanced imaging.** *Acad Radiol* 2012;19:1283–89
8. Kakeda S, Korogi Y, Yoneda T, et al. **A novel tract imaging technique of the brainstem using phase difference enhanced imaging: normal anatomy and initial experience in multiple system atrophy.** *Eur Radiol* 2011;21:2202–10
9. Yoneda T. **Triple-layer appearance of human cerebral cortices on phase difference enhanced imaging using 3D principle of echo shifting with a train of observations (PRESTO) sequence.** In: *Proceedings of the Annual Meeting of the International Society for Magnetic Resonance in Medicine*, Honolulu, Hawaii. April 18–24, 2009
10. Schaltenbrand G, Wahren W. **Microscopic series with fixed overlays for anatomic explanation.** In: Schaltenbrand G, Wahren W, eds. *Atlas for Stereotaxy of the Human Brain*. 2nd ed. Stuttgart: Thieme; 2005:51–55
11. Naidich TP, Duvernoy HM, Delman BN, et al. **Internal architecture of the brain stem with key axial sections.** In: Naidich TP, Duvernoy HM, Delman BN, et al, eds. *Duvernoy's Atlas of the Human Brain Stem and Cerebellum: High-Field MRI, Surface Anatomy, Internal Structure, Vascularization and 3D Section Anatomy*. Vienna: Springer-Verlag; 2009:53–94
12. Andrews TJ, Halpern SD, Purves D. **Correlated size variations in human visual cortex, lateral geniculate nucleus, and optic tract.** *J Neurosci* 1997;17:2859–68
13. Winer JA. **The human medial geniculate body.** *Hear Res* 1984; 15:225–47
14. Abduljalil AM, Schmalbrock P, Novak V, et al. **Enhanced gray and white matter contrast of phase susceptibility-weighted images in ultra-high-field magnetic resonance imaging.** *J Magn Reson Imaging* 2003;18:284–90
15. Duyn JH, van Gelderen P, Li TQ, et al. **High-field MRI of brain cortical substructure based on signal phase.** *Proc Natl Acad Sci U S A* 2007;104:11796–801
16. Marques JP, Maddage R, Mlynarik V, et al. **On the origin of the MR image phase contrast: an in vivo MR microscopy study of the rat brain at 14.1 T.** *Neuroimage* 2009;46:345–52
17. Zhong K, Leupold J, von Elverfeldt D, et al. **The molecular basis for gray and white matter contrast in phase imaging.** *Neuroimage* 2008;40:1561–66
18. He X, Yablonskiy DA. **Biophysical mechanisms of phase contrast in gradient echo MRI.** *Proc Natl Acad Sci U S A* 2009;106:13558–63
19. Li W, Wu B, Avram AV, et al. **Magnetic susceptibility anisotropy of human brain in vivo and its molecular underpinnings.** *Neuroimage* 2012;59:2088–97
20. Horton JC, Landau K, Maeder P, et al. **Magnetic resonance imaging of the human lateral geniculate body.** *Arch Neurol* 1990;47:1201–06
21. Fujita N, Tanaka H, Takanashi M, et al. **Lateral geniculate nucleus: anatomic and functional identification by use of MR imaging.** *AJNR Am J Neuroradiol* 2001;22:1719–26
22. Devlin JT, Sillery EL, Hall DA, et al. **Reliable identification of the auditory thalamus using multi-modal structural analyses.** *Neuroimage* 2006;30:1112–20